3-D analytical migration velocity analysis I: Two-step velocity estimation by reflector-normal update

Zhaobo Meng*, Norman Bleistein,† and Kay D. Wyatt‡

* *Center for Wave Phenomena, Colorado School of Mines; now Phillips Petroleum Company*
† *Center for Wave Phenomena, Colorado School of Mines*
‡ *Phillips Petroleum Company*

ABSTRACT

In this paper, we study 3-D reflector-normal approach to analytical migration velocity analysis (AMVA). A new way to measure the migration misfits, called the reflector-normal misfits, is proposed. The reflector-normal misfits vanish as long as the migration velocity model is true, regardless of the complexity of the model. It is shown that the conventional (vertical) misfit (z-misfit) based migration velocity update is only accurate for small dips. Based on reflector-normal misfits, we design two-step reflector-normal velocity update algorithms that impose no dip limits. These "interpolation-type" velocity update algorithms are unconditionally stable, and alleviate both misfit picking errors and migration errors. The AMVA algorithms proposed in this paper are applied to both a synthetic land 3-D dataset and a 3-D streamer dataset acquired in the Gulf of Mexico.

Introduction

Conventional common image gather (CIG) migration velocity analysis (MVA) approaches are derived under the assumptions of (1) lateral velocity homogeneity; (2) small offset and (3) small dip (Al-Yahya, 1989; MacKay & Abma, 1992). Liu & Bleistein (1995) introduced analytical migration velocity analysis (AMVA) derived only under the assumption of small dip. However, Meng & Bleistein (1999) demonstrated mathematically that, for offset-MVA, large offset is needed to avoid velocity/depth tradeoff. This makes Liu and Bleistein's AMVA (1995) approach a robust tool to resolve both velocity and depth. However, since all the above traditional approaches are derived under the assumption of small dips, estimation error increases with increasing dips.

Here, we extend to 3-D the 2-D AMVA technique of Liu & Bleistein (1995) and Liu (1995; 1997). Moreover, similar to Audebert *et al.* (1997), this 3-D AMVA approach imposes no dip limits. Here are some highlights of this AMVA approach:

First, based on ray theory, we show that the alignment of the (vertical) image (z-image) in a common image gather (CIG), *widely* used in practice (Al-Yahya, 1989; Deregowski, 1990; MacKay & Abma, 1992; Stork, 1992; Wyatt, 1995), is only valid for reflectors with small dips, and that error increases with increasing dip. This complies with the normal-ray approach by Audebert *et al.* (1997).

Second, unconditionally stable two-step reflector-normal velocity update algorithms are developed. A linearization technique is applied to solve the non-linear parameter estimation problem built for velocity estimation. The two-step *interpolation-type* algorithms first introduced as a 2-D approach by Liu & Bleistein (1995), are extended to 3-D. This interpolation-type approach reduces the inaccuracy of misfit picks noted by Zhang & McClellan (1994) and enhances stability when compared with the traditional single-step *extrapolation-type* algorithms. In addition, it alleviates the migration errors. The cost of this approach is comparable to the single-step algorithms.

To test the proposed reflector-normal velocity update algorithms, the approach is applied to both a synthetic 3-D land dataset and a 3-D streamer dataset acquired in the Mahogany field, Gulf of Mexico.

For MVA in complicated media, the proposed two-step reflector-normal velocity update algorithms can be viewed as first-step effort. It is recommended that a velocity gradient estimation (Meng *et al.*, 1999a) be applied after the velocity estimation.

Two-step reflector-normal velocity update

A practical strategy first introduced by Liu & Bleistein (1995) for a 2-D flat layered model with a constant background velocity is adopted in this paper. Liu & Bleistein (1995) used two migration velocities, $c_<$ and $c_>$, where, compared to the true velocity, c^*, $c_< < c^* < c_>$. The velocity to be updated is an interpolated value using these two trial velocities, $c_<$ and $c_>$. Such a scheme is called a *two-step algorithm* and is unconditionally stable (Liu & Bleistein, 1995).

We may write the updated velocity, c_{update}, as a linear combination of the two trial migration velocities as

$$c_{update} = \alpha c_< + (1-\alpha)c_>. \tag{1}$$

Then, following the Appendix, the interpolating weight, α, is given by the following equation

$$\alpha = \frac{c_> \delta L_>}{c_> \delta L_> - c_< \delta L_<} \tag{2}$$

and

$$1-\alpha = \frac{c_< \delta L_<}{c_< \delta L_< - c_> \delta L_>}, \tag{3}$$

where, $\delta L_<$ and $\delta L_>$ are the measured differences in the reflector-normal misfits as introduced in the Appendix. Since ideally $\delta L_< < 0$ and $\delta L_> > 0$, both α and $1-\alpha$ are positive. It follows that the sum of them is guaranteed to be 1, even in the presence of strong noise.

With details introduced in the Appendix, once the parameter α is obtained, equation (A24), or equation (A25), gives the zero-offset reflector-normal misfits, $\widehat{L}_<$, or $\widehat{L}_>$. Thus, equation (A10) gives the updated reflector

$$\mathbf{x}_{update} = \mathbf{x}_< - \widehat{L}_< \mathbf{n}, \tag{4}$$

or equivalently,

$$\mathbf{x}_{update} = \mathbf{x}_> - \widehat{L}_> \mathbf{n}. \tag{5}$$

Here, $\mathbf{x}_<$ and $\mathbf{x}_>$ are the post-migration imaged points with respect to the two trial velocities, $c_<$ and $c_>$. $\mathbf{n}$ is the normal vector to the reflecting subsurface.

The above algorithms are derived for constant background models with general reflecting subsurface. For more complicated models, these algorithms are used iteratively to obtain a final model. The estimated model can then be used as a starting model for a more accurate (and perhaps less stable) algorithm, such as the velocity gradient estimation algorithms introduced in Meng *et al.* (1999a), if necessary.

3-D land synthetic data test

In this section, the two-step reflector-normal velocity estimation algorithms are tested on a 3-D synthetic land dataset.

To fully test the reflector-normal velocity estimation, as well as the velocity gradient estimation to be reported in Meng *et al.* (1999a), we built a three-layered synthetic model of 15km×15km×2km. As shown in Figure 1, a constant velocity, $v = 1,500$m/s, is used for layer one. For layer two, the velocity is represented as

$$v(x,y,z) = v_0(x,y) + v_z(x,y)(z - z_0(x,y)), \tag{6}$$

where $z_0(x,y) \le z < z_1(x,y)$. $v_0(x,y) = v(x,y,z_0(x,y)+)$ is the varying initial velocity at horizon one, $z = z_0(x,y)$, as shown in Figure 2. $v_z(x,y)$ is the varying vertical velocity gradient, as shown in Figure 2 in Meng *et al.* (1999a). Horizon one, $z = z_0(x,y)$, and horizon two, $z = z_1(x,y)$, are dome-shaped. Both are 100m shallower at their centers than on their edges. Figure 3 shows the target horizon, horizon two. The total number of nodes for horizontal discretization in AMVA is 100 × 100 with a uniform spacing of 150m. However, AMVA is only applied to 20 ≤ix≤ 80 and 20 ≤iy≤ 80 (ix and iy are the node numbers), due to the lack of data at the boundaries. The aim of this synthetic data test is to examine how well the AMVA approach resolves, (i) the top horizon velocity, $v_0(x,y)$; (ii) the depth of horizon two, $z_1(x,y)$ and (iii) the vertical velocity gradient in layer two, $v_z(x,y)$, which is reported in Meng *et al.* (1999a).

Kirchhoff forward modeling (Wyatt *et al.*, 1997; Branham *et al.*, 1998) by the Huygen-Fresnel principle is applied to generate the 3-D synthetic land dataset needed for the tests. A 3-D land survey geometry is simulated.

The two-step reflector-normal velocity estimation algorithm requires two initial models to start the estimation process. To avoid "extrapolation", this is preferable to have both a velocity-too-low model and a velocity-too-high model, but this is not a rigid requirement.

For the velocity-too-low model, we used a low constant velocity, $v_0^< = 2,000$m/s, as the initial guess for the top horizon velocity, $v_0(x,y)$, with a relative error of at least 20%. Since a low initial top horizon velocity is used, a shallower initial constant depth, $z_1^< = 1,328$m with a relative error of about -11.5% on the edges of horizon two, is used for horizon two. At this point, we assume that we do not have *a priori* information about the vertical velocity gradient for this synthetic dataset. Thus, we assume that the initial vertical velocity gradient for layer two and below is zero: $v_z^< = 0$.

For the velocity-too-low model, horizon-based

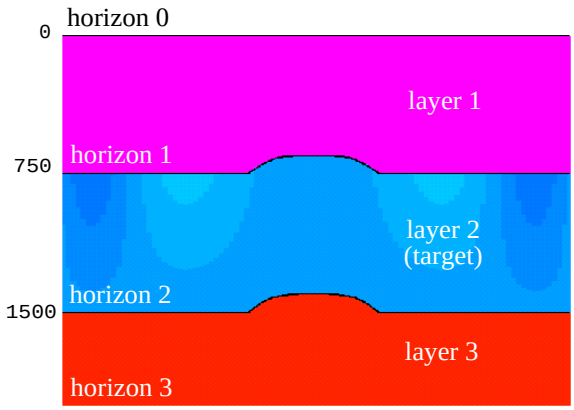

Figure 1. A profile view of the true synthetic model used for synthetic tests. A constant top horizon velocity, $v = 1,500$m/s, is used in layer one; a varying top horizon velocity of the target layer, $v_0(x,y)$, and a varying vertical velocity gradient, $v_z(x,y)$, (Figure 2) are used for layer two. Horizon one, $z = z_0(x,y)$, and horizon two, $z = z_1(x,y)$, are dome-shaped, and both are 100m shallower at the centers than on the edges. The depth of horizon one, $z_0(x,y)$, is 750m in depth at its edges and 650m in depth at its center. The depth of horizon two, $z_1(x,y)$, is $1,500$m in depth on its edges and $1,400$m in depth at its center.

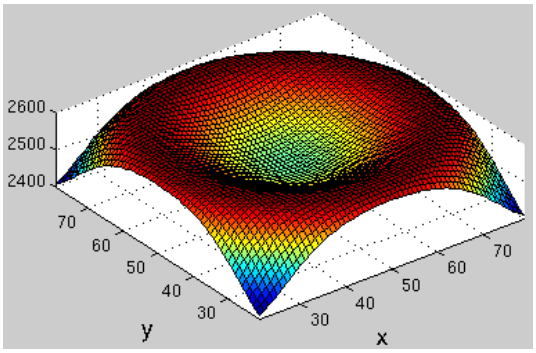

Figure 2. The true velocity at the top horizon of layer two, the target layer ($20 \leq$ix≤ 80 and $20 \leq$iy≤ 80).

prestack depth imaging (HPSDM) (Wyatt *et al.*, 1997) is applied to the synthetic data to output a subset of imaged data within a window vertically centered at the target horizon (imaging horizon) (Wyatt *et al.*, 1997).

For a closer look at the CIGs, Figure 4 shows two sample CIGs obtained from this velocity-too-low model. The upward-bending of the image in both CIGs indicates that the initial top horizon velocity in the target layer is too low. For this data test, Figure 4 also indicates that the imaging horizon (the center line) is too deep at CIG ix=50, iy=50 (right CIG in Figure 4). Thus, one can apply an optional base adjustment using equation (4). The model after this base adjustment is called the "base-adjusted model". After this base adjustment and

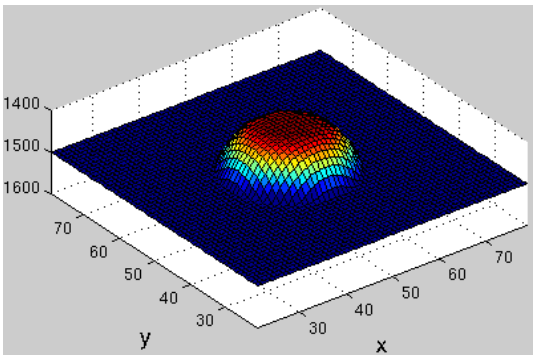

Figure 3. The true depth of horizon two, the base horizon of the target layer, $z_1(x,y)$, in the imaging area. The base horizon is at $1,400$m in depth at the center $(50,50)$ $1,500$m in depth on the edges.

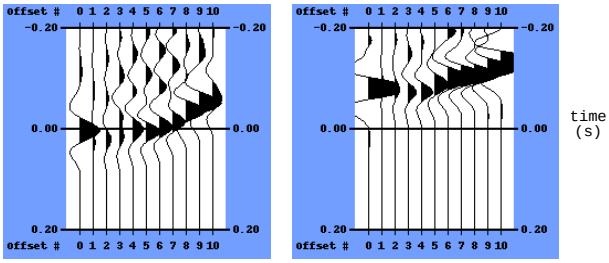

Figure 4. Sample CIGs extracted from line 50 for the velocity-too-low initial model. The CIG on the left is located at ix=20, iy=50; while the CIG on the right is located in the center of the model at ix=50, iy=50. The observed upward bending indicates that the initial top horizon velocity is too low, the measured near-offset reflector-normal misfits at ix=50, iy=50, $\widehat{L}_<$, indicates that the HPSDM imaging horizon is too deep at ix=50, iy=50.

applying new HPSDM, the base horizon image in the zero-offset CIGs (Figure 6) are aligned much better than before.

To initiate the two-step velocity estimation algorithms, in addition to the velocity-too-low model, one also needs a velocity-too-high model. As an initial guess building our model, we used a high top horizon velocity, $v_0^> = 3,000$m/s, (with a relative error of at least 20%) for layer two. Thus, a deeper initial depth for horizon two, $z_0^> = 1,638$m (with a relative error of 9.2% at the edges of horizon two) is used. The initial guess for the vertical velocity gradient of layer two is zero, $v_z^> = 0$.

For this velocity-too-high model, the same procedure is applied as for the velocity-too-low model. We are now ready to apply the two-step reflector-normal velocity estimation.

HPSDM is again applied to both the base-adjusted, velocity-too-low model and the base-adjusted, velocity-too-high model. For each model, a subset of imaged data

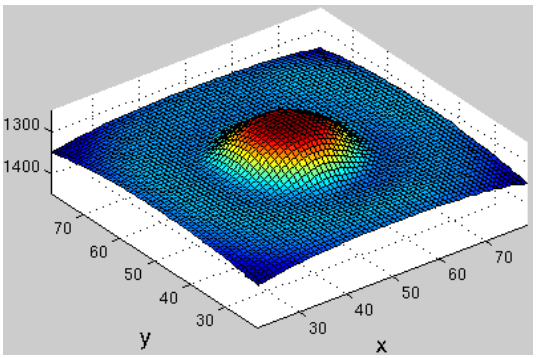

Figure 5. The adjusted base horizon (right), $z_1^<(x,y)$, by using the measured zero-offset reflector-normal misfits, $\widehat{L}_<$, for the velocity-too-low model.

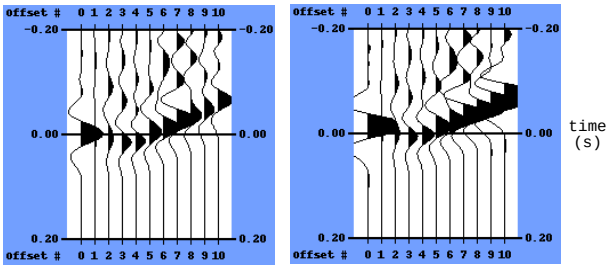

Figure 6. Two sample CIGs extracted from line 50 for the velocity-too-low initial model. The CIG on the left is at ix=20, iy=50; while the CIG on the right is at ix=50, iy=50. The observed upward-bending in both CIGs indicates that the initial top horizon velocity is too low.

centered at the new imaging horizon of layer two is sorted into CIGs. In the CIG panels, the differences in reflector-normal misfits for both models, $\delta L_<$ and $\delta L_>$ (introduced in (A26) and (A27), respectively), are picked automatically (Wyatt *et al.*, 1997). Equations (2) and (3), or (A30) and (A31), give weights for top horizon velocity interpolation, and equation (1) gives the updated top horizon velocity. Equation (4) adjusts the imaging horizon along the reflector-normal direction.

After the first iteration of the two-step velocity estimation, the top horizon velocity is still too low in the target layer, layer two. Thus, this new model, the velocity-still-too-low model, should replace the original velocity-too-low model, and the velocity-too-high model remains, so that a new pair of velocity-too-low model and velocity-too-high model are found, and another iteration of the two-step velocity estimation are then applied. Figures 8 and 9 show the adjusted depth of the imaging horizon, $z_1^3(x,y)$, and the updated velocity of the target layer, $v_0^2(x,y)$, respectively. Figure 10 shows two sample CIGs showing no residual curvature with increasing offset. The results show that the two-step velocity estimation gives

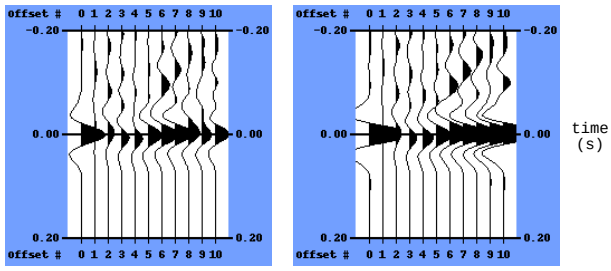

Figure 7. Two sample CIGs extracted from line 50 after the first iteration of two-step velocity estimation. The left is a sample CIG at ix=20, iy=50; the right is a CIG at ix=50, iy=50.

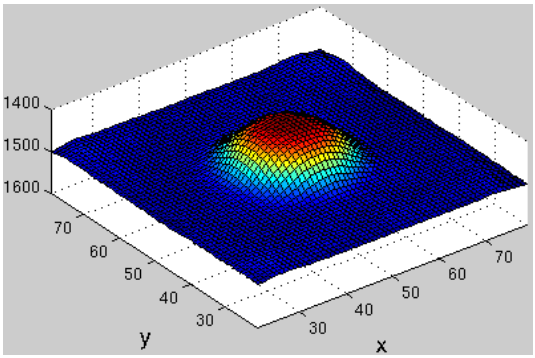

Figure 8. The depth of the imaging horizon of the target layer, $z_1^4(x,y)$, after base adjustment and two iterations of the two-step velocity estimation.

a good estimate for the depth, even with a wrong vertical velocity gradient for the synthetic data tests. Up to this point, both the top horizon velocity and the imaging horizon are updated properly. Velocity gradient estimation will be applied to this dataset and be reported in Meng *et al.* (1999b). Figure 11 shows the error in the updated velocity. The relatively large errors are partly due to the *wrong* initial zero-vertical velocity gradients, $v_z^0 = 0$.

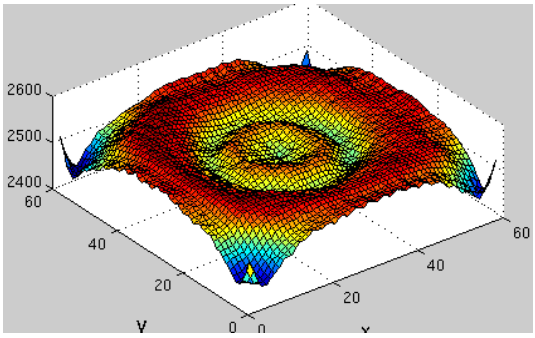

Figure 9. The updated top horizon velocity, $v_0^2(x,y)$, after two iterations of the two-step velocity estimation.

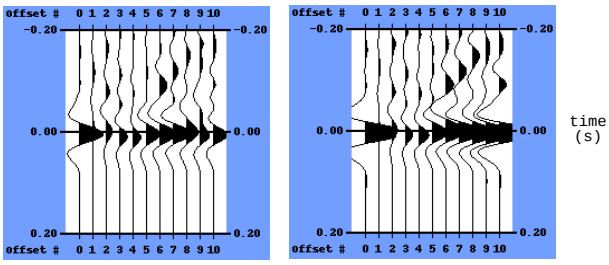

Figure 10. Two sample CIGs extracted from line 50 for the model after two iterations of two-step velocity estimation. The left is a CIG at ix=20, iy=50; the right is a CIG at ix=50, iy=50.

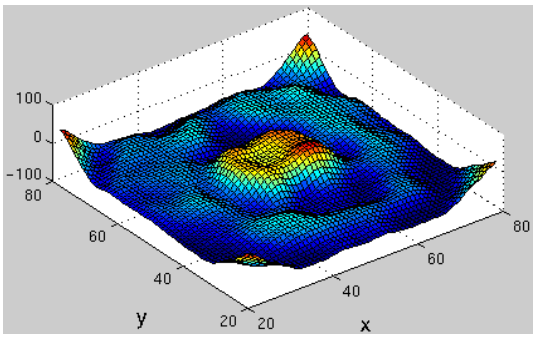

Figure 11. The error in top horizon velocity after two iterations of velocity estimation. The relative errors are mostly within 1% for the center area, while larger errors are seen at the boundaries where there are not enough data available.

The 3-D Mahogany marine data tests

In this last section, the two-step velocity and depth estimation algorithms are tested on a land 3-D synthetic dataset. Now, we report on a test of the algorithms on field data–a 3-D dataset (Westcott *et al.*, 1995) from a marine streamer shot over the Mahogany field in the Gulf of Mexico.

To start over velocity estimation, we used the original model obtained from a conventional DMO-based velocity analysis. Figure 12 shows a profile view of the initial model, Profile A.

HPSDM (Wyatt *et al.*, 1997) shows that the velocity in layer two is too low. Thus, we choose layer two as the first target layer. We can move down later to deeper layers in sequence.

After the base adjustment to both models, the near-offset images are aligned to the imaging horizons. Figure 13 shows some sample CIGs at ix=75, iy=59 for the base-adjusted, velocity-too-low model (left) and for the base-adjusted, velocity-too-high model. The center (zero) lines in the figure represent the base horizons. Next, the differences in reflector-normal misfits for both models, $\delta L_<$ and $\delta L_>$, are picked.

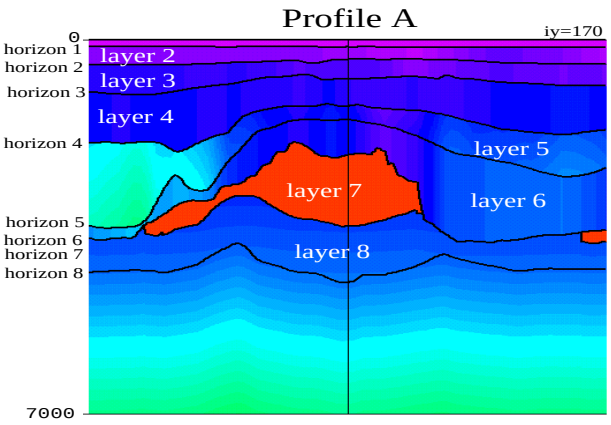

Figure 12. Profile A of the initial Mahogany model for the velocity-too-low model. This initial model is obtained by using a conventional DMO-based velocity analysis algorithm.

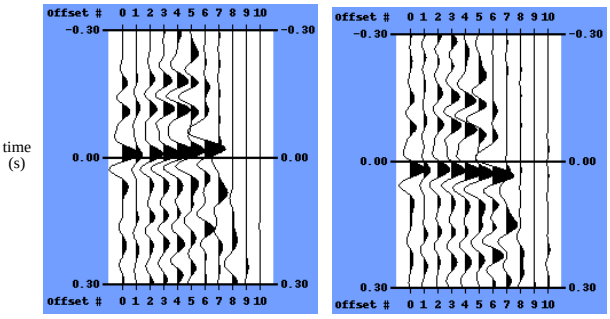

Figure 13. Sample CIGs at ix=75, iy=59 for the base-adjusted, velocity-too-low model (left) and for the base-adjusted, velocity-too-high model. The center lines in the figure represent the imaging horizons.

Finally, we applied the two-step velocity estimation. Figure 14 shows the near-offset image of Profile A, and Figure 15 shows the 400 – 500m offset image of Profile A. The alignment of both the near-offset and the 400 – 500m offset CIGs with the imaging horizon indicates that both the velocity and the base horizon of the target layer have been properly corrected. We found it is necessary to apply the two-step reflector-normal velocity update to deeper layers, too.

Conclusions

We have proposed a reflector-normal velocity update approach that imposes no dip limits. We show that the traditional (vertical) z-misfit based MVA causes increasing errors with increasing dips.

The proposed two-step velocity update algorithms are designed for simultaneous velocity update and depth adjustment. The two-step algorithms are uncondition-

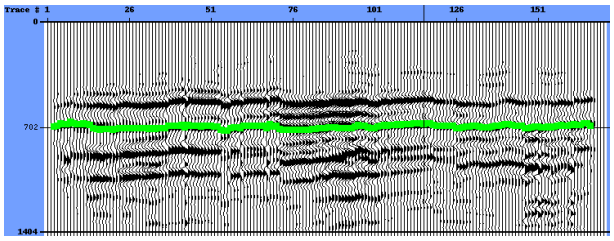

Figure 14. The near-offset HPSDM image in the imaging window for Profile A after one iteration of two-step velocity estimation for layer two. The alignment of the base-horizon image (marked) with the base-horizon (the center line in the figure) indicates a match between the base horizon of the target layer and the imaging-horizon.

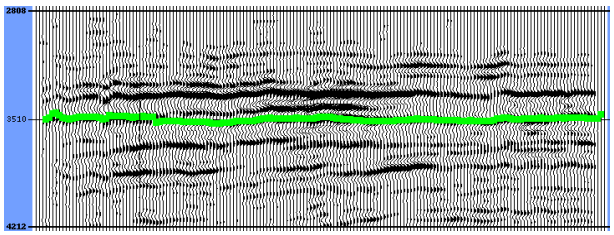

Figure 15. The $400-500$m offset HPSDM image in the imaging window for Profile A after one iteration of two-step velocity estimation for layer two. The alignment of the $400-500$m offset base-horizon image with the imaging-horizon (the center line) in this figure, and the near offset base-horizon with the imaging-horizon (the center line) in Figure 14), indicates that both the velocity and the base horizon of the target layer are properly updated.

ally stable, and alleviate the instability problem in misfit picking noted by Zhang and McClellan (1994). The unconditional convergence makes the two-step reflector-normal velocity update approach desirable for velocity estimation in complicated areas, where a single-step approach may fail to converge.

For a complex medium, the reflector-normal velocity update algorithms may be viewed as a first-step effort, in which a velocity gradient estimation (Meng *et al.*, 1999a) may be needed after the velocity update.

To verify the two-step reflector-normal velocity update approach, the proposed algorithms are applied on both a 3-D synthetic dataset and a 3-D marine dataset acquired in the Gulf of Mexico. The flattened CIGs indicate that both models are properly updated.

Acknowledgments

We are thankful for the numerous comments and advice from Paul Valasek, Bob Heaton, Jennifer Swanson, Yunqing Shen, Brian K. Macy of Phillips Petroleum Company. The authors greatly acknowledge the financial support by Phillips and by the Office of Naval Research, through CWP, as well as the partial support by the sponsors of the Consortium Project on Seismic Inverse Methods for Complex Structures at the Center for Wave Phenomena, Colorado School of Mines. Finally, we acknowledge the permission from the Geco-Prakla partnership to use the Mahogany, Gulf of Mexico, dataset and to publish the results.

References

Al-Yahya, K. 1989. Velocity analysis by iterative profile migration. *Geophysics*, **54**, 718–729.

Audebert, Francois, Diet, Jean-Paul, Jones, Iran F., & Zhang, Xiaoming. 1997. CRP-Scans: 3D PreSDM Velocity Analysis via Zero-Offset Tomographic Inversion. *Pages 1805–1808 of: 67th Annual Internat. Mtg., Soc. Expl. Geophys., Expanded Abstracts.*

Branham, K., Wyatt, K. D., Valasek, P. A., & Cass, K. R. 1998. Velocity and illumination studies from horizon-based PSDM–A case study. *In: 69th Annual Internat. Mtg., Soc. Expl. Geophys., Expanded Abstracts.*

Deregowski, S. M. 1990. Common-offset migrations and velocity analysis. *First Break*, **8**, 225–234.

Liu, Z. 1995. Migration velocity analysis. *Pages 1–88 of: Ph. D. thesis, Colorado School of Mines.*

Liu, Z. 1997. An analytical approach to migration velocity analysis. *Geophysics*, **62**, 1238–1249.

Liu, Z., & Bleistein, N. 1995. Migration velocity analysis: Theory and an iterative algorithm. *Geophysics*, **60**, 142–153.

MacKay, S., & Abma, R. 1992. Imaging and velocity estimation with depth-focusing analysis. *Geophysics*, **57**(12), 1608–1622.

Meng, Z. 1999. Tetrahedral Based Earth Models, Ray Tracing in Tetrahedral Models and Analytical Migration Velocity Analysis. *Pages 1–180 of: Ph. D. thesis, Colorado School of Mines, CWP-296.*

Meng, Z., & Bleistein, N. 1999. On Velocity/Depth Ambiguity in 3-D migration velocity analysis. *This report.*

Meng, Z., Bleistein, N., & Valasek, P. A. 1999a. 3-D Analytical Migration Velocity Analysis II: Velocity Gradient Estimation. *This report.*

Meng, Z., Bleistein, N., & Valasek, P. A. 1999b. 3-D Analytical Migration Velocity Analysis II: Velocity Gradient Estimation. *In: 69th Annual Internat. Mtg., Soc. Expl. Geophys., Expanded Abstracts*, vol. 99.

Stork, C. 1992. Reflection tomography in the postmigrated domain. *Geophysics*, **57**, 680–592.

Westcott, Mark E., Leach, Mark C., Wyatt, Kay D., Valasek, Paul A., & Branham, Keith L. 1995. Mahogany: Seismic technology leading to the first economic subsalt field. *Pages 1161–1164 of: 65th Annual Internat. Mtg., Soc. Expl. Geophys., Expanded Abstracts*, vol. 95.

Wyatt, K. D., Valasek, P. A., Wyatt, S. B., & Heaton, R. M. 1997. Velocity and illumination studies from horizon-based PSDM. *Pages 1801–1804 of: 67th Annual Internat. Mtg., Soc. Expl. Geophys., Expanded Abstracts*, vol. 97.

Wyatt, K. D. et. al. 1995. Rapid velocity estimation using horizon-based 3-D prestack depth migration. *In: Research workshop: "Velocity Estimation for 3-D Imaging", 65th Annual Internat. Mtg., Soc. Expl. Geophys*, vol. 65.

Zhang, J., & McMechan, G. A. 1994. 3-D transmission tomography using wide aperture data for velocity estimation of irregular salt bodies. *Geophysics*, **59**(10), 1620–1630.

APPENDIX A: Reflector-normal update–AMVA without dip limits

To study AMVA, we start from the zero-offset/azimuth imaging conditions. We denote by $\mathbf{x}$ a 3-D reflection point $\mathbf{x} = (x_1, x_2, x_3)$. Let $\mathbf{x}_s = (x_{1s}, x_{2s}, x_{3s})$ denote the source positions and $\mathbf{x}_g = (x_{1g}, x_{2g}, x_{3g})$ denote the geophone positions, both located on the datum surface (not necessarily horizontal). Let $\boldsymbol{\xi} = (\xi_1, \xi_2, \xi_3 \equiv \gamma, \xi_4 \equiv h)$ be the horizontal coordinates (the acquisition parameters), where γ is the azimuthal angle and h the half offset. For example, in the common offset/azimuth gather, ξ_1 and ξ_2 are the horizontal coordinates of the midpoint the source/geophone pairs in inline and crossline directions, respectively; in the common shot gather, ξ_1 and ξ_2 are the horizontal coordinates of the geophone positions (Liu & Bleistein, 1995); etc.

Following Liu & Bleistein (1995) and Meng (1999), let $\tau_s(\mathbf{x}_s; \mathbf{x})$ denote the traveltime from source $\mathbf{x}_s$ to a subsurface point, $\mathbf{x}$, and let $\tau_g(\mathbf{x}; \mathbf{x}_g)$ denote the traveltime from $\mathbf{x}$ back to receiver, $\mathbf{x}_g$. Then, the zero-time imaging condition can be interpreted as

$$\tau(\mathbf{x}_s, \mathbf{x}, \mathbf{x}_g) \equiv \tau_s(\mathbf{x}_s; \mathbf{x}) + \tau_g(\mathbf{x}; \mathbf{x}_g) = t(\boldsymbol{\xi}). \tag{A1}$$

Here, $\tau(\mathbf{x}_s, \mathbf{x}, \mathbf{x}_g)$ is the total travel time, $t(\boldsymbol{\xi})$ is the observed travel time, $\boldsymbol{\xi}$ is the acquisition parameter. Differentiating equation (A1) with respect to $\xi_3 = \gamma$ and $\xi_4 = h$ yields

$$\frac{\partial \tau_s}{\partial x_{js}} \frac{\partial x_{js}}{\partial \gamma} + \frac{\partial \tau_g}{\partial x_{jg}} \frac{\partial x_{jg}}{\partial \gamma} = \frac{\partial t}{\partial \gamma} \tag{A2}$$

and

$$\frac{\partial \tau_s}{\partial x_{js}} \frac{\partial x_{js}}{\partial h} + \frac{\partial \tau_g}{\partial x_{jg}} \frac{\partial x_{jg}}{\partial h} = \frac{\partial t}{\partial h}, \tag{A3}$$

respectively. From these conditions, we obtain the zero-offset/azimuth imaging conditions (Meng, 1999)

$$n_j \frac{\partial x_j}{\partial \gamma} = \frac{v}{2\cos\theta} \left(\frac{\partial t}{\partial \gamma} - \frac{\partial \tau_s}{\partial x_{js}} \frac{\partial x_{js}}{\partial \gamma} - \frac{\partial \tau_g}{\partial x_{jg}} \frac{\partial x_{jg}}{\partial \gamma} \right) \tag{A4}$$

and

$$n_j \frac{\partial x_j}{\partial h} = \frac{v}{2\cos\theta} \left(\frac{\partial t}{\partial h} - \frac{\partial \tau_s}{\partial x_{js}} \frac{\partial x_{js}}{\partial h} - \frac{\partial \tau_g}{\partial x_{jg}} \frac{\partial x_{jg}}{\partial h} \right). \tag{A5}$$

Here, v is the true velocity; θ is the half-opening angle (half scattering angle); $\mathbf{x} = (x_1, x_2, x_3)$ is the imaged point; $\mathbf{n} = (n_1, n_2, n_3)$ is the *reflector-normal*–normal to the imaged reflector (Fig A1). Equations (A4) and (A5) form the basis for the post-migration AMVA. Basically, equations (A4) and (A5) indicate that, if the true velocity has been used in migration (thus equations (A2) and (A3) hold), the right hand sides of equations (A4) and (A5) vanish. Which can be interpreted as, the imaged point, $\mathbf{x}$, does not vary with respect to γ and h along the reflector-normal direction, $\mathbf{n}$. This is true *regardless of the complexity of the model*. More interpretation of these equations can be found in Meng (1999).

We need to be careful about what parameters to use to characterize MVA. In appendix C in Meng (1999), it is shown that, for simple background models, among other acquisition parameters, $\boldsymbol{\xi}$, offset and azimuth completely characterize MVA. Thus, it is safe to define the *reflector-normal derivatives* with respect to γ and h, $\Gamma(\gamma, h; v, \mathbf{x})$ and $H(\gamma, h; v, \mathbf{x})$, as functions of azimuth γ and half offset h

$$\Gamma(\gamma, h; v, \mathbf{x}) = n_j \frac{\partial x_j}{\partial \gamma}, \tag{A6}$$

$$H(\gamma, h; v, \mathbf{x}) = n_j \frac{\partial x_j}{\partial h}. \tag{A7}$$

Similarly, we introduce the *reflector-normal derivative*, $C(c; \boldsymbol{\xi}, \mathbf{x})$, with respect to the migration velocity, c, as (Meng, 1999)

$$C(c; \boldsymbol{\xi}, \mathbf{x}) \equiv n_j \frac{\partial x_j}{\partial c} = \frac{t(\boldsymbol{\xi})}{2\cos\theta} > 0. \tag{A8}$$

Mathematically, the above equation reveals some desirable characteristics of the reflector-normal derivative with respect to the migration velocity. The quantity on the right in (A8) remains absolutely positive. That is, for migration with a constant velocity, the reflector-normal derivative with respect to the migration velocity is *monotonic* in the migration velocity c, which means, stability can be easily guaranteed for reflector-normal update.

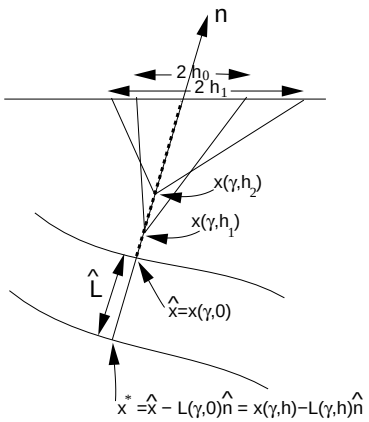

Figure A1. Cartoon for reflector-normal perturbation. Here, $\mathbf{x}(\gamma, h)$ is the near-offset HPSDM imaged point with a wrong migration velocity; $\mathbf{x}^*$ is the zero-offset imaged point with the correct migration velocity. $\widehat{L}$ is the zero-offset reflector-normal perturbation due to the difference between the migration velocity from the true velocity.

The reflector-normal misfits, $L(\gamma, h; c)$

In this section, we quantify the reflector-normal perturbation and refer to it as the reflector-normal misfits.

For constant background velocity, we can write the measured traveltime, $t(\gamma, h; c^*)$, as

$$t(\gamma, h; c^*) = \frac{\rho_s^*(\gamma, h) + \rho_g^*(\gamma, h)}{c^*}. \tag{A9}$$

Here, c^* is the true velocity that is unknown; $\rho_s^*(\gamma, h)$ and $\rho_g^*(\gamma, h)$ are the lengths of ray paths to the source and receiver corresponding to the true velocity, c^*, respectively.

Suppose that c is the erroneous migration velocity, while $\rho_s(\gamma, h)$ and $\rho_g(\gamma, h)$ are the lengths of ray paths to the source and receiver corresponding to the erroneous migration velocity, c, respectively. To make the AMVA work iteratively, let us assume that the migration velocity, c, is *close to* the true velocity, c^*. In addition, let us only consider the case for the perturbation to the reflector in the reflector-normal direction, $\mathbf{n}$. This last assumption also guarantees that the normal remains unperturbed. Now, we can write the imaged point, $\mathbf{x}(\gamma, h; c)$, as a perturbation to the true reflector, $\mathbf{x}^*$, in the reflector-normal direction, $\mathbf{n}$, as

$$\mathbf{x}(\gamma, h; c) = \mathbf{x}^* + L(\gamma, h; c)\mathbf{n}, \tag{A10}$$

or, one can write the *amount* of perturbation, as

$$L(\gamma, h; c) = (\mathbf{x}(\gamma, h; c) - \mathbf{x}^*) \cdot \mathbf{n}. \tag{A11}$$

Let us call the amount of perturbation, $L(\gamma, h; c)$, the *reflector-normal misfits* with respect to the azimuth, γ, and half offset, h, due to the use of erroneous migration velocity, c. From the analysis in the previous sections, when the true migration velocity, c^*, is used, the reflector-normal misfits should vanish for all azimuth, γ, and half offset, h. That is,

$$L(\gamma, h; c^*) \equiv 0. \tag{A12}$$

Two-step reflector-normal update algorithms

In this section, we derive the two-step velocity estimation algorithms that are accurate for constant background models with arbitrary reflecting subsurface. The algorithm is designed as an iterative AMVA scheme for more complicated models. The two-step velocity estimation algorithms are recommended to be used to provide initial guesses for further velocity gradient estimation (Meng *et al.*, 1999a), if necessary. Thus, *stability* is of high priority for two-step velocity estimation, while precision is of high priority for velocity gradient estimation (Meng *et al.*, 1999a).

Under the assumption of constant true velocity, c^*, and constant migration velocity, c, with arbitrary reflecting subsurface, we can rewrite equation (A9),

$$\frac{\rho_s^*(\gamma, h) + \rho_g^*(\gamma, h)}{c^*} = \frac{\rho_s(\gamma, h) + \rho_g(\gamma, h)}{c}. \tag{A13}$$

Notice that, from (A11), clearly the reflector-normal misfits are unmeasurable, because the true image, $\mathbf{x}^*$, in (A11) is unknown. Fortunately, one can measure the differences in reflector-normal misfits at different offsets and azimuths. For this reason, it is useful to introduce the *zero-offset reflector-normal misfits*. Since for zero-offset, there is no azimuth dependence (the azimuth value does not matter at zero-offset), the zero-offset reflector-normal misfits, are denoted as

$$\widehat{L}(c) = L(\gamma, 0; c) = (\widehat{\mathbf{x}}(c) - \mathbf{x}^*) \cdot \mathbf{n}. \tag{A14}$$

Here, the zero-offset imaged point, $\widehat{\mathbf{x}}(c)$, is defined as

$$\widehat{\mathbf{x}}(c) = \mathbf{x}(\gamma, 0; c). \tag{A15}$$

Notice that, $\widehat{\ }$ in this paper indicates that the quantity is associated with the zero-offset. Thus, the differences in reflector-normal misfits can be introduced as

$$\delta L(\gamma, h; c) = L(\gamma, h; c) - \widehat{L}(c). \tag{A16}$$

In practice, the *differences in reflector-normal misfits*, $\delta L(\gamma, h; c)$, is measured.

For zero-offset data, denote, $\widehat{\rho}_< \equiv \widehat{\rho}_{s<} \equiv \widehat{\rho}_{g<}$, as the zero offset one-way ray path length from the source/receiver to the imaged point, $\widehat{\mathbf{x}}_<(c_<) = \mathbf{x}(\gamma, 0; c_<)$, using the low migration velocity $c_<$. Similarly, denote, $\widehat{\rho}_> \equiv \widehat{\rho}_{s>} \equiv \widehat{\rho}_{g>}$, as the zero-offset one-way ray path length from the source/receiver to the imaged point, $\widehat{\mathbf{x}}_>(c_>) = \mathbf{x}(\gamma, 0; c_>)$, using the high migration velocity $c_>$. Furthermore, denote, $\rho^* \equiv \widehat{\rho}^* \equiv \widehat{\rho}_s^* \equiv$

$\widehat{\rho}_g^*$, as the (zero-offset) one-way ray path length from source/receiver to the true reflector. Following the previous discussion, for zero-offset data, all the ray paths line in the reflector-normal direction, $\mathbf{n}$. In other words,

$$\frac{\widehat{\rho}_<}{c_<} = \frac{\widehat{\rho}^*}{c^*} = \frac{\widehat{\rho}_>}{c_>}. \tag{A17}$$

From equation (A14), for the low migration velocity $c_<$, we denote the zero-offset reflector-normal misfits

$$\widehat{L}_<(c_<) = L(\gamma, 0; c_<) = (\widehat{\mathbf{x}}_<(c_<) - \mathbf{x}^*) \cdot \mathbf{n}. \tag{A18}$$

Since the zero-offset ray paths lie in the direction of the normal, $\mathbf{n}$, one can write

$$\widehat{\rho}_< = \widehat{\rho}^* + \widehat{L}_<, \tag{A19}$$

and for migration velocity $c_>$, we denote the zero-offset reflector-normal misfits

$$\widehat{L}_>(c_>) = L(\gamma, 0; c_>) = (\widehat{\mathbf{x}}_>(c_>) - \mathbf{x}^*) \cdot \mathbf{n}. \tag{A20}$$

Since both the zero-offset ray paths lie in the direction of the normal, $\mathbf{n}$, as well, one can write

$$\widehat{\rho}_> = \widehat{\rho}^* + \widehat{L}_>. \tag{A21}$$

From equation (A17), if one writes the true velocity, c^*, as a linear combination of the two trial migration velocities $c_<$ and $c_>$,

$$c^* = \alpha c_< + (1-\alpha) c_>, \tag{A22}$$

then, one can also write

$$\widehat{\rho}^* = \alpha \widehat{\rho}_< + (1-\alpha)\widehat{\rho}_>. \tag{A23}$$

$\widehat{\rho}^*$ is the zero-offset ray path length lying between the two imaged points associated with the pair of migration velocities, $c_<$ and $c_>$. Since zero-offset ray path lies in the reflector-normal direction, $\widehat{\rho}^*$ determines the zero-offset reflector-normal misfit, $\widehat{L}_<$ and $\widehat{L}_>$, thus determines the adjusted base horizon by equation (4) or (5). Here, α is the unknown parameter (weight) to be determined. Equations (A22) and (A23) simultaneously determine the updated velocity and the updated imaged point associated with the base horizon. Substituting $\widehat{\rho}^*$ in (A23) into equations (A19) and (A21), respectively, yields the reflector-normal zero-offset misfits

$$\widehat{L}_< = \widehat{\rho}_< - \widehat{\rho}^* = (1-\alpha)(\widehat{\rho}_< - \widehat{\rho}_>) \tag{A24}$$

and

$$\widehat{L}_> = \widehat{\rho}_> - \widehat{\rho}^* = \alpha(\widehat{\rho}_> - \widehat{\rho}_<). \tag{A25}$$

With only zero-offset data, it is impossible to estimate α, thus impossible to resolve the perturbations to both the velocity and the base horizon from equations (A22) and (A23). To obtain the interpolation weight, α, one needs to measure some differences in reflector-normal misfits $\delta L_<(\gamma, h; c_<)$ and $\delta L_>(\gamma, h; c_>)$ associated with both the velocities, $c_<$ and $c_>$. For the low migration velocity $c_<$, we measure the differences in reflector-normal misfits

$$\delta L_<(\gamma, h; c_<) = L_<(\gamma, h; c_<) - \widehat{L}_<(c_<). \tag{A26}$$

Similarly, for the high migration velocity $c_>$, we measure the differences in reflector-normal misfits

$$\delta L_>(\gamma, h; c_>) = L_>(\gamma, h; c_>) - \widehat{L}_>(c_>). \tag{A27}$$

With some mathematical derivation (Meng, 1999), we have

$$\delta L_< = (1-\alpha)\frac{c_< - c_>}{c_<}\left(\frac{\rho_{s<} + \rho_{g<}}{2\cos\theta_<} - \widehat{\rho}_<\right) \tag{A28}$$

and

$$\delta L_> = \alpha\frac{c_> - c_<}{c_>}\left(\frac{\rho_{s>} + \rho_{g>}}{2\cos\theta_>} - \widehat{\rho}_>\right). \tag{A29}$$

Now, from the above two equations, after "normalizing" α and $1-\alpha$ (so that the sum of them is guaranteed to be one, even in the presence of strong noise in the measured misfits $\delta L_<$ and $\delta L_>$), we have

$$\alpha = \frac{c_>\delta L_>}{c_>\delta L_> - c_<\delta L_<\beta}, \tag{A30}$$

and thus,

$$1-\alpha = \frac{c_<\delta L_<}{c_<\delta L_< - c_>\delta L_>\beta^{-1}}. \tag{A31}$$

Here, coefficient

$$\beta = \frac{(\rho_{s>} + \rho_{g>})/\cos\theta_> - 2\widehat{\rho}_>}{(\rho_{s<} + \rho_{g<})/\cos\theta_< - 2\widehat{\rho}_<}. \tag{A32}$$

can be estimated from the other parameters by raytracing or analytically (Meng, 1999). Figure A2 gives a geometric interpretation of this quantity. Notice that

$$\lim_{c_> - c_< \to 0} \beta = 1. \tag{A33}$$

In other words, $\beta = 1$ is a good approximation when the velocity perturbation is small. Thus, if we approximate $\beta \approx 1$, we have the formula (2) similar to (48) in Liu & Bleistein (1995), except that here we use reflector-normal misfits, rather than z-misfits.

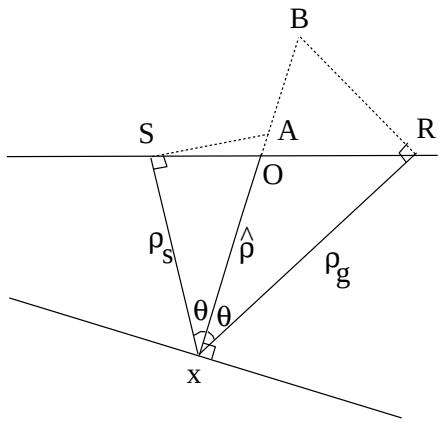

Figure A2. Cartoon for the ray paths for determining the coefficient β. Here, X is the imaged point, S and R are the source and receiver positions, respectively. θ is the half-opening angle at the imaged point X, ρ_s and ρ_g are the length of the ray paths from the imaged point to the source and receiver, respectively, i.e., $\rho_s = \overline{XS}$, $\rho_g = \overline{XR}$. $\widehat{\rho}$ is the (half) zero-offset ray path length, that is, $\widehat{\rho} = \overline{XO}$. The coefficient β in equation (A32) is the ratio of the quantity, $\overline{XA} + \overline{XB} - 2\overline{XO} = \overline{OA} + \overline{OB}$, for the high velocity model, to, this quantity for the low velocity model.